

# Numerical Investigation of Separation Control for Wing Sections

A. Gross\* and H.F. Fasel†

The University of Arizona, Tucson, AZ 85721

Received date 15/2/2012; Accepted date 9/4/2013

For Reynolds numbers that are typical for general aviation aircraft separation is typically turbulent. In this paper the question is addressed if flow control strategies that are successful at low-Reynolds number conditions remain effective at higher Reynolds numbers. Towards this end hybrid simulations based on a one-equation renormalization group model were carried out for a modified NACA643-618 airfoil at a chord Reynolds number of one million. For ten degrees angle of attack a short laminar separation bubble develops near the leading edge and the flow separates turbulent from the suction side downstream of the leading edge bubble. Active flow control by harmonic blowing through a spanwise slot was investigated. The control was found to be only mildly effective or even counterproductive. In particular, the disturbances that were introduced by the control were only weakly amplified or even dampened. The unresolved eddy viscosity in the separated boundary layer lowers the effective Reynolds number and makes the flow less unstable or even stable with respect to two-dimensional disturbances. As a consequence of this, higher blowing ratios are required compared to flow control at low-Reynolds number conditions where the shear-layer instability is stronger.

## 1. INTRODUCTION

The Mean Aerodynamic Chord (MAC) Reynolds number for general aviation aircraft at cruise is in the order of several million. At such high Reynolds numbers separation is typically turbulent. Separation control strategies such as pulsed vortex generator jets and harmonic blowing and suction through slots were successfully employed for controlling laminar separation at low Reynolds number conditions. Examples are separation control for low-pressure turbine blades [1–3] and laminar airfoils [4–7]. In this paper the question is addressed if harmonic blowing through a slot is also effective at higher Reynolds numbers. The Reynolds number scalability of a flow control strategy can be investigated by keeping an appropriate dimensionless parameter (such as the momentum coefficient) constant and then determining how dimensionless performance parameters (such as the lift and drag coefficient) change when the Reynolds number is altered (e.g. Thake et al. [7]). Of particular interest is also the question if similar physical mechanisms can be exploited for an efficient flow control when the Reynolds number is varied.

Several years ago a research project was initiated at the University of Arizona involving dynamically scaled models of general aviation aircraft, [8] such as the Aeromot 200S Super Ximango motor glider, which has a modified NACA 64<sub>3</sub>-618 airfoil (the modified airfoil has a higher maximum lift coefficient than the original NACA 64<sub>3</sub>-618). Two-dimensional (2D) wing sections were tested in the wind and water tunnel for Reynolds numbers between 64,200 and  $Re = 322,000$ , the model (1/5 scale) cruise Reynolds number based on MAC. [5, 6, 9] The experiments were complemented by simulations for  $Re = 64,200$  [4, 10] and  $Re = 322,000$  [11, 12]. The full-size cruise Reynolds number is 3.2 million. Thake et al. [7] investigated separation control by steady vortex generator jets for the original NACA 64<sub>3</sub>-618 airfoil. Four different Reynolds numbers,  $Re = 64,200$ , 180,000, 1 million, and 4 million were considered. Although the blowing ratio for the highest Reynolds number was slightly smaller than for the other cases, the control effectiveness appeared to decrease with increasing Reynolds number when the blowing ratio was held constant.

---

\*agross@email.arizona.edu

†faselh@email.arizona.edu

The present investigations are for the modified NACA 64<sub>3</sub>-618 airfoil of the Aeromot 200S motor glider. Simulations were carried out for a chord Reynolds number of one million. Direct Numerical Simulations (DNS) for this Reynolds number are computationally very expensive. In DNS no turbulence modeling is invoked and all scales of fluid motion are resolved. In Large Eddy Simulation (LES) the subgrid scales are modeled which lowers the computational expense. However, because of the near-wall grid resolution requirement even LES can be quite expensive. In Reynolds-Averaged Navier-Stokes (RANS) all turbulent scales are modeled. Hybrid turbulence models blend between LES and RANS to take advantage of the favorable properties of both approaches. Typically, RANS is employed near walls. Away from walls, depending on the local physical grid resolution, the model reverts to LES or DNS. For the hybrid simulations presented in this paper, a one-equation Renormalization Group (RG) model proposed by De Langhe et al. [13, 14] was employed.

## 2. SIMULATION STRATEGY

### 2.1. Hybrid Turbulence Model

For the one-equation Renormalization Group (RG) model by De Langhe et al. [13, 14] a transport equation for the turbulence dissipation rate,  $\varepsilon$ ,

$$\frac{\partial \rho \varepsilon}{\partial t} + \frac{\partial \rho u_i \varepsilon}{\partial x_i} = \frac{\partial}{\partial x_i} \left[ \left( \mu + 1.39 \mu_T \right) \frac{\partial \varepsilon}{\partial x_i} \right] + \frac{\mu + \mu_T}{\rho} [\min(\Lambda_c, \Lambda)]^2 \left( \frac{4}{3} P_k - 2 \rho \varepsilon \right), \quad (1)$$

with production term,  $P_k = \tau_{ij}^T u_{i,j}$ , and eddy viscosity,

$$\mu_T = \mu \left\{ \left[ 1 + \frac{0.1 \rho^3 \varepsilon}{\mu^3} \max(0, \Lambda_c^{-4} - \Lambda^{-4}) \right]^{\frac{1}{3}} - 1 \right\}, \quad (2)$$

is solved. Here,  $\Lambda_c = \max(\pi/L_\Delta, \pi/2.2y)$ , where  $y$  denotes the wall distance, and  $\Lambda = 0.215(\rho^3 \varepsilon / \mu^3)^{0.25}$ . The filter width is taken as the cell diagonal,  $L_\Delta = \sqrt{\Delta x^2 + \Delta y^2 + \Delta z^2}$ . The Reynolds stresses are computed from the Boussinesq-approximation (linear eddy viscosity model),  $\tau_{ij}^T = 2\mu_T(S_{ij} - u_{k,k}\delta_{ij}/3)$ .

### 2.2. Change in Grid Resolution

The unresolved turbulence energy spectrum can be modeled by the Kolmogorov energy spectrum,

$$E(\kappa) = C_k \varepsilon^{\frac{2}{3}} \kappa^{-\frac{5}{3}}, \quad (3)$$

where  $\kappa = 2\pi/L$  is a wavenumber. The Kolmogorov constant is taken as 1.44 [15]. The unresolved Turbulence Kinetic Energy (TKE),  $k$ , is obtained by integration from the Kolmogorov length scale,

$$L_k = \left( \frac{\nu^3}{\varepsilon} \right)^{\frac{1}{4}}, \quad (4)$$

to a multiple,  $n_\Delta$ , of the grid length scale,  $L_\Delta$ ,

$$k = \int_{2\pi/n_\Delta L_\Delta}^{2\pi/L_k} E(\kappa) d\kappa = \frac{3}{2} C_k \left( \frac{\varepsilon}{2\pi} \right)^{\frac{2}{3}} \left[ (n_\Delta L_\Delta)^{\frac{2}{3}} - L_k^{\frac{2}{3}} \right]. \quad (5)$$

Assuming that the dissipation rate,  $\varepsilon$ , is almost independent of the grid length scale (most of the dissipation takes place at the smallest scales and the dissipation at the resolved scales is neglected), the derivative of the unresolved TKE with respect to the grid length scale becomes

$$\frac{\partial k}{\partial L_\Delta} = C_k \left( \frac{n_\Delta \varepsilon}{2\pi} \right)^{\frac{2}{3}} L_\Delta^{-\frac{1}{3}}. \quad (6)$$

For the present results,  $n_\Delta = 2$ . Artificial turbulent velocity fluctuations are “injected” or “seeded” for

$$-u_i \frac{\partial L_\Delta}{\partial x_i} \frac{\partial k}{\partial L_\Delta} > 0, \quad (7)$$

to maintain the correct turbulence kinetic energy balance [12]. Similar approaches have been proposed earlier by e.g. Batten et al [16]. Although the one-equation RG model does not employ a transport equation for the unresolved TKE, Eq. 7 can be evaluated since  $\varepsilon$  and therefore also  $\partial k / \partial L_\Delta$  (Eq. 6) are known. The artificial velocity fluctuations are obtained from a synthetic turbulence model by Rogallo [17].

### 2.3. Discretization

The present investigations were carried out with a research computational fluid dynamics code that was developed in our laboratory [18]. The Favre-averaged compressible Navier-Stokes and turbulence model equations are solved in the finite volume formulation. The convective terms of the Navier-Stokes equations were discretized with a 5<sup>th</sup>-order-accurate upwind scheme. The viscous terms were discretized with 4<sup>th</sup>-order accuracy. The turbulence model equations were discretized with second-order accuracy. A second-order-accurate implicit Adams-Moulton scheme was employed for time-integration.

### 2.4. Boundary Conditions

The wall boundary condition for the RG model is

$$\varepsilon = 0.22 \frac{u_\tau^4}{\nu} = 0.22 \frac{\mu}{\rho} \left( \frac{\partial u}{\partial y} \right)^2. \quad (8)$$

Walls were considered to be adiabatic. Periodicity conditions were applied in the spanwise direction. A characteristics-based non-reflecting boundary condition [19] was employed at the freestream boundary.

### 2.5. Non-dimensionalization and Coordinate System

Velocities, length scales, and eddy viscosity were made dimensionless with the freestream velocity,  $v_\infty$ , the airfoil chord,  $c$ , and the freestream molecular viscosity,  $\mu_\infty$ , respectively. Time was made dimensionless with  $c/v_\infty$  and frequencies were made dimensionless with  $v_\infty/c$ .

### 2.6. Computational Domains

All simulations are for the modified NACA 64<sub>3</sub>-618 airfoil of the Aeromot 200S motor glider. A Poisson grid generator [20] was employed for obtaining O-grids with high orthogonality and smoothness. The number of cells in the circumferential, wall-normal, and spanwise directions as well as the spanwise grid extent,  $L_z$ , are provided in Tab. 1. Because of their much lower computational expense, for flow control parameter studies 2-D hybrid simulations were carried out in addition to the 3-D simulations. For the 2-D simulations the filter width  $L_\Delta$  was computed assuming  $\Delta z = 0.00625$ . The grid extent in the radial direction was more than  $20c$ . A close-up of the computational grid is provided in Fig. 1.

Because a hybrid approach was employed for the present simulations a grid resolution study in the strict sense is not possible. When the grid resolution is increased the turbulence model

Table 1. Spanwise domain extent,  $L_z$  and number of cells in the circumferential, radial, and spanwise direction ( $N_x$ ,  $N_y$ , and  $N_z$ ).

$L_z$	$N_x$	$N_y$	$N_z$
0	600	200	–
0.15	600	200	32
0.3	600	200	64
0.6	600	200	128

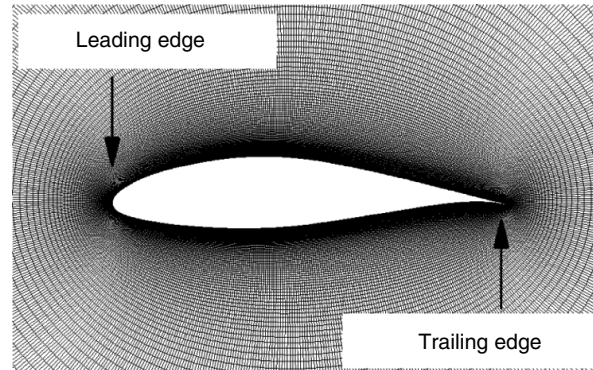


Figure 1. Closeup of computational grid.

contribution will be reduced and vice versa. In other words, by changing the grid resolution the performance of the hybrid model in the fine and coarse grid limit can be tested. Such a model verification, however, is not subject of the present study. For the present investigations it is assumed that the model is working correctly. Two concerns remain with respect to the grid resolution: (1) Because the present interest is in flow control that excites unsteady flow structures, the computational grid has to be fine enough to resolve the energetic flow structures. The results in section III indicate that this is the case. (2) The near-wall grid resolution has to be less than one to resolve the viscous sublayer. For the grids used the near-wall grid resolution is in fact lower than one (Fig. 2a) and, as a result, the laminar sublayer is well resolved (Fig. 2b).

## 2.7. Reynolds Number and Angle of Attack

The Reynolds number based on MAC for the full-size Aeromot 200S Super Ximango is 3.2 million at cruise (110 knots) and approximately 1.5 million at minimum sink speed (52 knots). Wind tunnel data for  $Re = 1$  million are available for the original NACA 64<sub>3</sub>-618 airfoil [7] but not for the modified NACA 64<sub>3</sub>-618 airfoil. Therefore, reference data for the present hybrid simulations were obtained using XFOil [22]. This panel method combined with boundary layer corrections provides accurate boundary layer data and aerodynamic coefficients for attached and mildly separated airfoil flows. Because of the models invoked for the calculation of separated flows, the accuracy of XFOil results for large angles of attack is limited. Ultimately, experimental data are required for a validation of the present hybrid simulations. All XFOil results were obtained with a critical N-factor of 9 and assuming either free transition or fixed transition at the leading edge ( $x = 0$ ). XFOil results with free transition show that compared to  $Re = 322,000$  (the 1/5 scale model cruise Reynolds number [8]) the slope of the lift curve is increased for  $Re = 1$  million and the maximum lift coefficient is larger (Fig. 3). For  $a > 7deg$  the lift curve deviates from the linear lift curve indicating trailing edge separation. A successful active control of the trailing edge separation would increase lift at high angles of attack and thus improve airplane performance. In this paper, results from hybrid simulations for a chord Reynolds number of one million and for angles of attack of  $\alpha = 10, 20, \text{ and } 30$  deg are presented.

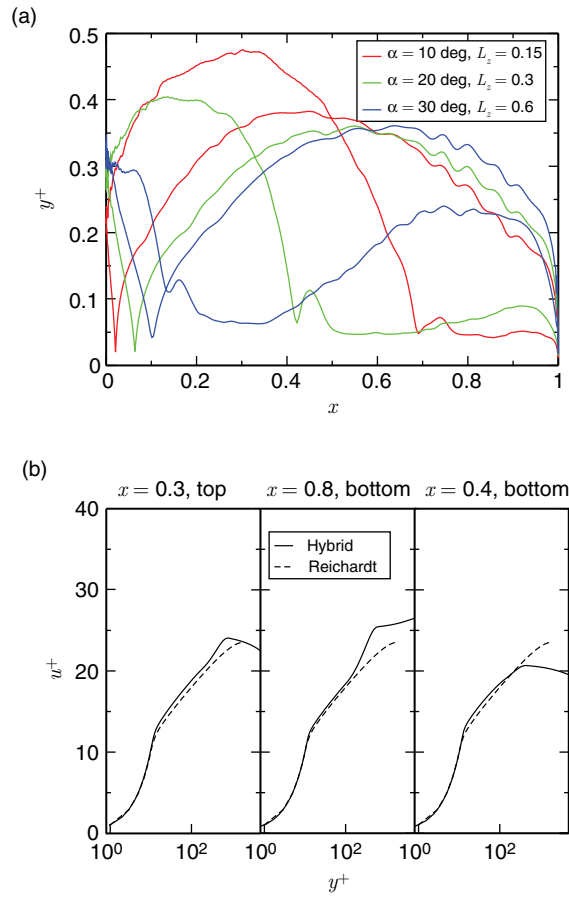


Figure 2. Uncontrolled flow. (a) Near-wall grid resolution in wall units and (b) velocity profiles in wall units for  $\alpha = 10$  deg (comparison with Reichardt profile [21]).

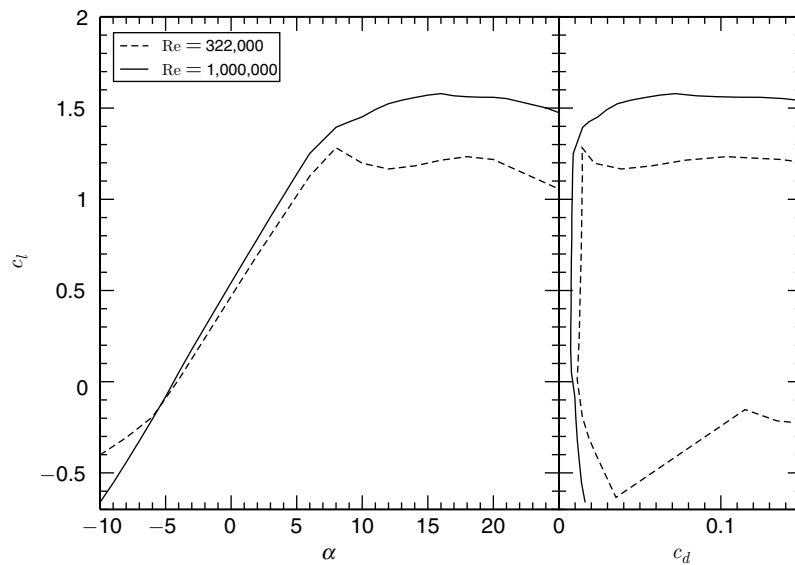


Figure 3. Lift curve and drag polar as predicted by XFOil for  $Re = 322,000$  and  $Re = 1$  million.

Table 2. Dimensionless time intervals for initial transients and time-averages.

$\alpha$	$L_z$	case	initial transient	time-average
10	0.15	uncontrolled	14	4.5
		$f = 1, A = 0.1, \varphi = 90 \text{ deg}$	3	3
		$f = 4, A = 0.1, \varphi = 90 \text{ deg}$	4.5	1.5
	0 (2-D)	uncontrolled	7	5
		$f = 1, A = 1, \varphi = 30 \text{ deg}$	2.5	2.5
		$f = 1, A = 4, \varphi = 30 \text{ deg}$	2.5	2.5
20	0.15	uncontrolled	6	4.5
		uncontrolled, no inj.	4	1
	0.3	uncontrolled	4.5	5
30	0.15	uncontrolled	7	1.5
	0.6	uncontrolled	2.5	1.5

## 2.8. Simulation Details

The computational timestep for the simulations was  $\Delta t = 0.0005$  and the maximum Courant-Friedrichs-Lewy number was about 8000. The freestream TKE was  $k_\infty = 10^{-6}$  which corresponds to a freestream turbulence intensity of  $Tu_\infty = \sqrt{2/3k_\infty} = 0.082\%$ . The freestream integral turbulence

length scale was  $l_{T_\infty} = 2 \times 10^{-4}$ , resulting in a freestream eddy viscosity of  $\mu_{T_\infty} = \sqrt{3/2} Re Tu_\infty l_{T_\infty} = 0.2$ . The freestream turbulence dissipation rate then becomes  $\varepsilon_\infty = c_\mu \rho_\infty k_\infty^2 / \mu_{T_\infty} = 4.5 \times 10^{-7}$ . The Mach and Prandtl numbers were 0.1 and 0.72, respectively, and the freestream temperature was  $T_\infty = 300K$ .

The time-averaging was initiated after the dimensionless aerodynamic forces had settled into time-periodic behavior with a steady mean. The simulations with flow control were started from the uncontrolled flow state. The time intervals for the initial transients and the time-averages are provided in Tab. 2.

## 3. RESULTS

### 3.1. Uncontrolled Flow

#### 3.1.1. Variation of Angle of Attack

Flow visualizations for the uncontrolled flow at  $\alpha = 10, 20$ , and  $30 \text{ deg}$  are provided in Fig. 4. The  $Q$  vortex identification criterion [24] which indicates areas where rotation dominates strain,

$$Q = \frac{1}{2} (W_{ij}W_{ij} - S_{ij}S_{ij}), \quad (9)$$

was employed for visualizing the vortical flow structures. Also included are iso-contours of the spanwise vorticity component,

$$\omega_z = \frac{\partial v}{\partial x} - \frac{\partial u}{\partial y}, \quad (10)$$

and skin friction lines computed from the time-averaged data. The width of the computational domain was increased for  $\alpha = 20$  and  $30 \text{ deg}$ . A linear stability analysis by Pierrehumbert and Widnall [23] showed that the spanwise wavelength of the most unstable fundamental secondary instability mode is two thirds the streamwise spacing of the spanwise vortices resulting from the primary instability. Estimates for the streamwise spacing of the spanwise vortices,  $l$ , can be obtained directly from the simulations (Fig. 4) and are provided in Tab. 3. The computed  $2/3l$  approximately match the spanwise domain extents employed for the present simulations.

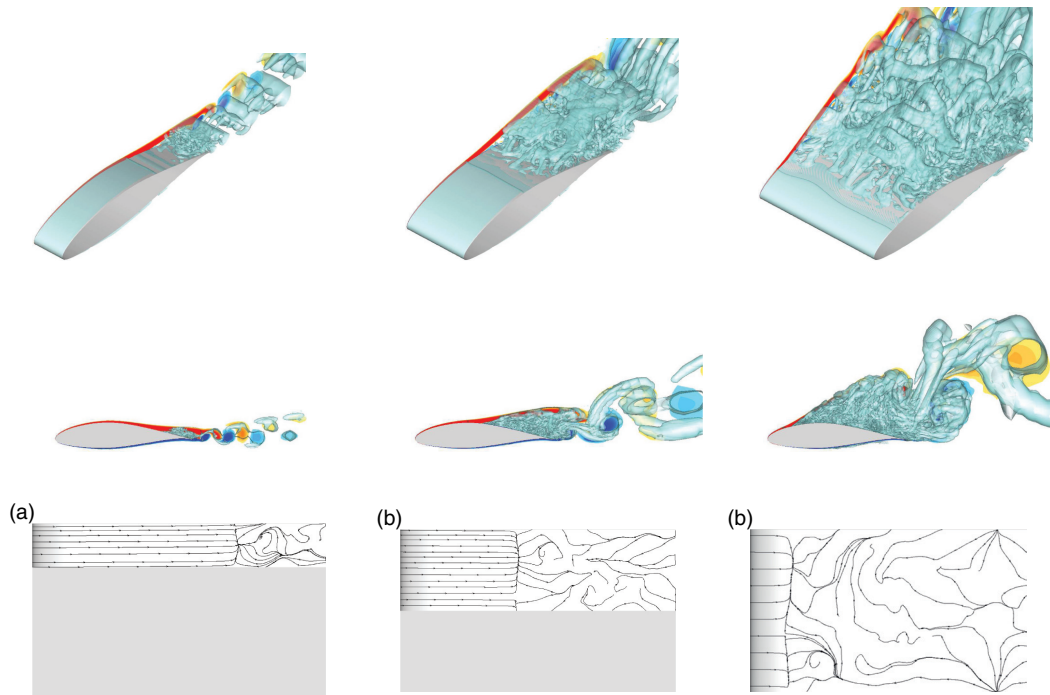


Figure 4. Uncontrolled flow. Iso-surfaces of  $Q = 1$ , iso-contours of spanwise vorticity,  $-20 < \omega_z < 20$ , and wall skin friction lines for a)  $\alpha = 10$  deg, b) 20 deg, and c) 30 deg.

Table 3. Approximate streamwise separation of spanwise vortices,  $l$ , and estimated spanwise wavelength of dominant secondary instability mode.

$\alpha$	$l$	$2/3l$
10 deg	0.17	0.11
20 deg	0.53	0.35
30 deg	0.89	0.60

The flow visualizations for  $\alpha = 10$  deg show trailing edge separation that moves upstream as the angle of attack is increased. Different from earlier low-Reynolds number simulations [4] no pronounced “roll up” of the separated boundary layer is apparent. For the low-Reynolds number simulations this “roll up” was attributed to a Kelvin-Helmholtz instability. Nevertheless, the present simulations indicate a distinct wake shedding that is reminiscent of a von Kármán vortex street. Also of interest is the fact that the separation line is slightly curved. Finally, it should be noted that the small-scale structures in the recirculation region underneath the separated boundary layer may be interpreted as coherent structures within a turbulent flow. The smallest dissipating scales are modeled in the hybrid RANS/LES approach.

Iso-contours of the unresolved eddy viscosity (using a logarithmic scale) are shown in Fig. 5. Elevated levels of the unresolved eddy viscosity for the pressure and suction side boundary layer indicate that the turbulence model “transitions” near the leading edge. For the suction side boundary layer the error made by the early transition of the model is small since in the experiments at high angles of attack a laminar separation bubble is naturally forming near the leading edge [7]. This laminar separation bubble “trips” the flow to turbulence. However, this is not the case for the boundary layer on the pressure side. While the boundary layer on the pressure side remains laminar in the experiment it is turbulent in the present hybrid simulations. To simulate this behavior in XFOIL, calculations were carried out where XFOIL was operated assuming fully turbulent boundary layers (denoted as “XFOIL turbulent”). To remedy this shortcoming of the hybrid model the transition points could be fixed (e.g., based on the  $e^N$  method) or a more elaborate

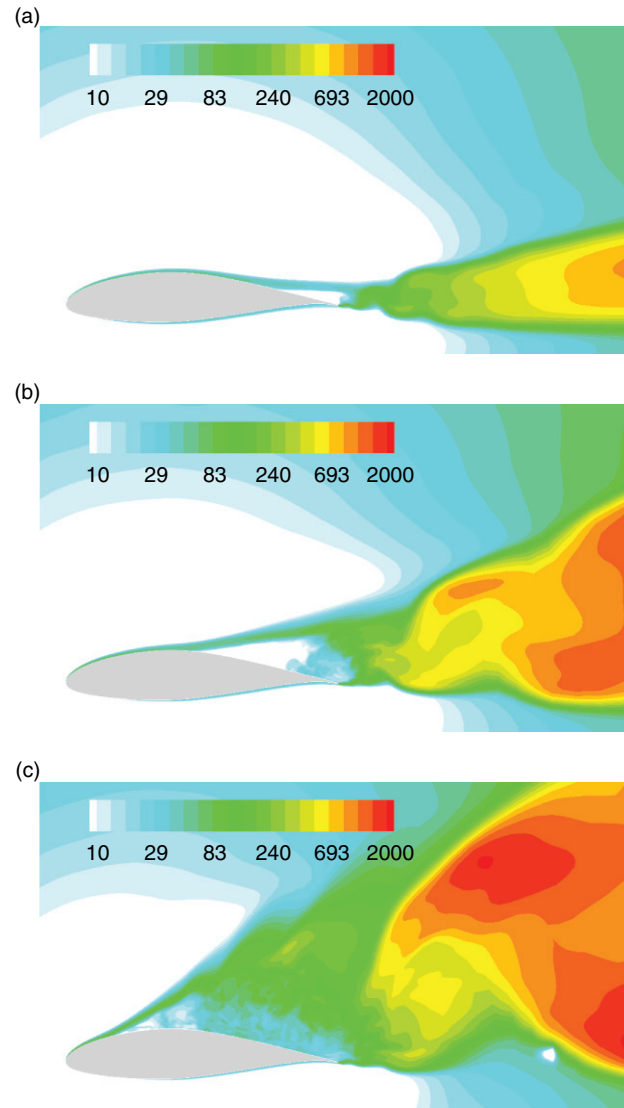


Figure 5. Uncontrolled flow. Iso-contours of unresolved eddy viscosity,  $\mu_T$ , for (a)  $\alpha = 10$  deg, (b) 20 deg, and (c) 30 deg.

underlying RANS model could be chosen that captures transition. Distributions of the wall pressure,

$$c_p = \frac{p - p_\infty}{\frac{1}{2} \rho_\infty v_\infty^2}, \quad (11)$$

and skin friction coefficient,

$$c_f = \frac{\mu \left. \frac{\partial u}{\partial y} \right|_{wall}}{\frac{1}{2} \rho_\infty v_\infty^2}, \quad (12)$$

are shown in Fig. 6. For  $\alpha = 10$  and 20 deg the wall pressure distributions agree well with the fully turbulent XFOil results. In both instances, XFOil predicts a leading edge laminar separation bubble, which transitions the suction side boundary layer. For  $\alpha = 30$  deg XFOil indicates leading edge stall. The hybrid simulations, on the other hand, predict separation near 15% chord. Several explanations may be offered for this mismatch: (1) XFOil predictions for very large  $\alpha$  are inaccurate. Ultimately, experimental reference data are required. (2) The hybrid model may need improvement. Laminar leading edge separation cannot be captured when the boundary layer is turbulent.

Iso-contours of the streamfunction,  $\Psi$ , ( $u = \partial\Psi/\partial y$ ;  $v = -\partial\Psi/\partial x$ ) computed from temporal and spanwise averages are provided in Fig. 7. As the angle of attack is increased the stagnation point shifts downstream (on the pressure side) and the separation moves upstream. In addition, the size of the wake increases. For  $\alpha = 30$  deg the wake is characterized by two counter-rotating vortices of comparable size.

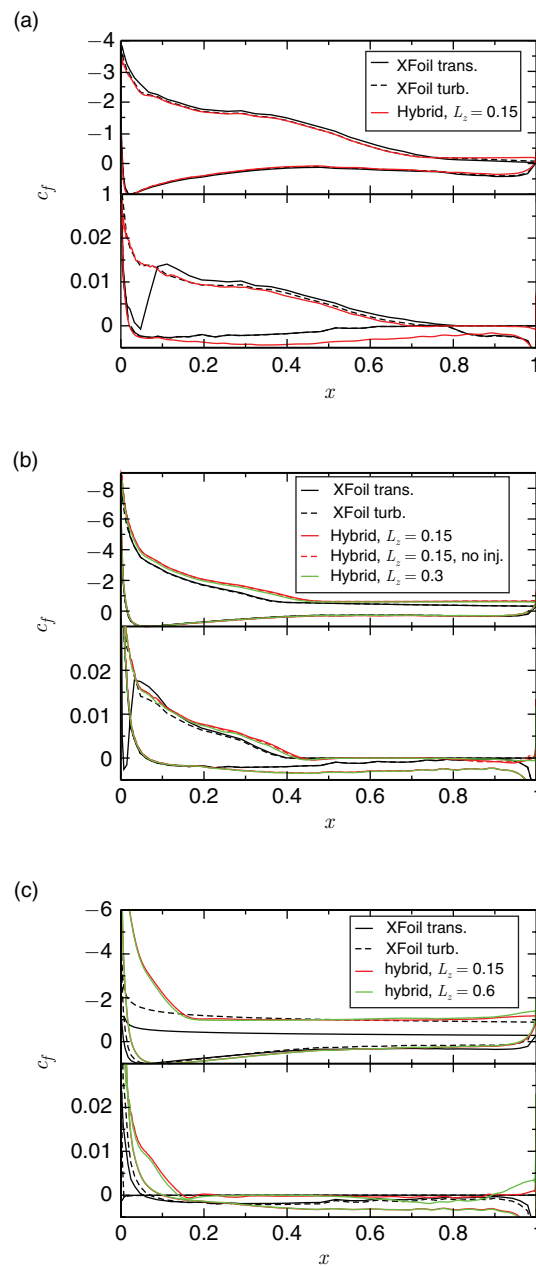


Figure 6. Uncontrolled flow. Wall pressure and skin friction coefficient for (a)  $\alpha = 10$  deg, (b) 20 deg, and (c) 30 deg.

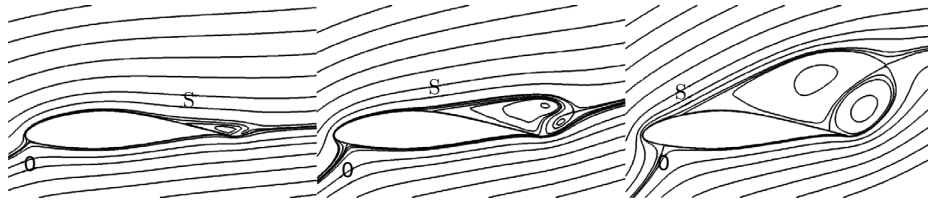


Figure 7. Uncontrolled flow. Streamfunction iso-contours for  $\alpha = 10$  deg (left), 20 deg (center), and 30 deg (right). “O”: Stagnation point, “S”: Mean separation point.

This flow pattern is typical for bluff body wakes. The second more downstream located vortex induces a meanflow on the airfoil surface that is directed towards the trailing edge for  $x > 0.9$ .

### 3.1.2. Domain Width Study

Additional simulations were carried out to determine the effect of the spanwise domain extent and the turbulence “injection” (Sec. II.B) on the mean flow characteristics. Results for  $\alpha = 20$  deg for two different domain widths ( $L_z = 0.15$  and  $L_z = 0.3$ ) are shown in Figs. 8 and 9. The instantaneous flow visualizations reveal no obvious differences between the various cases. The primary instability, the von

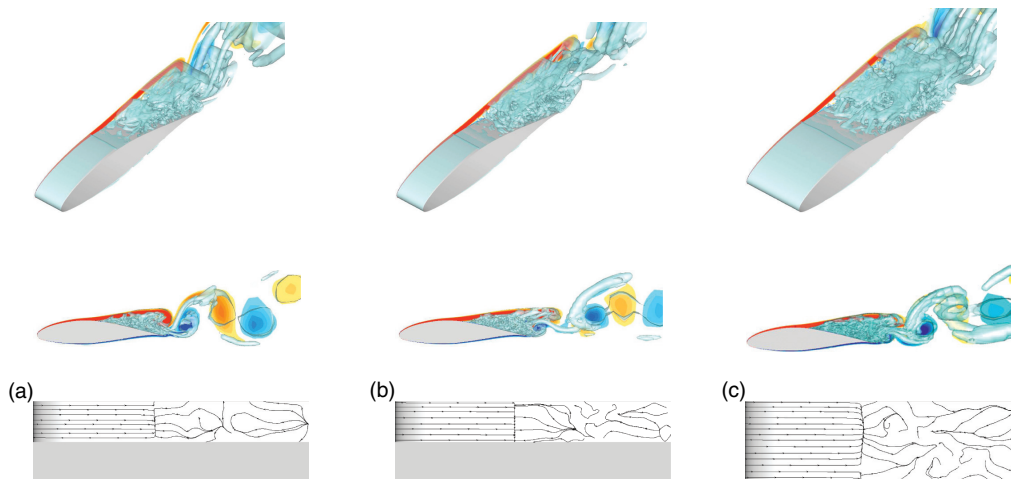


Figure 8. Uncontrolled flow for  $\alpha = 20$  deg. Iso-surfaces of  $Q = 1$ , iso-contours of spanwise vorticity,  $-20 < \omega_z < 20$ , and wall skin friction lines for (a)  $L_z = 0.15$ , (b)  $L_z = 0.15$  without “turbulence injection”, and (c)  $L_z = 0.3$ .

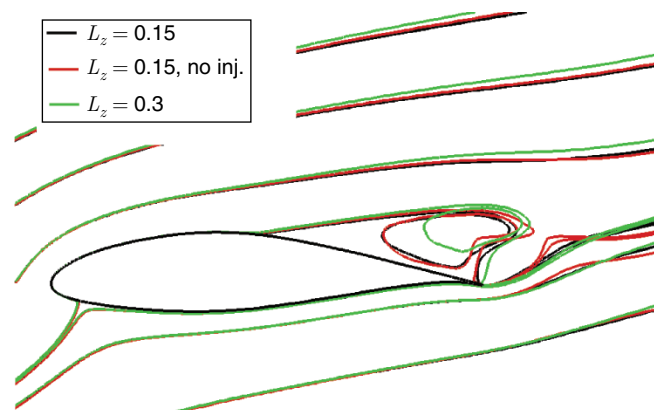


Figure 9. Uncontrolled flow. Streamfunction iso-contours for  $\alpha = 20$  deg.

Kármán wake shedding, is captured in all instances. When considering the time averages it can be seen that the separation line becomes almost straight when the turbulence “injection” is turned off (all other simulations were carried out with turbulence “injection”). For the narrow domain the curvature of the separation line is reduced compared to the simulation for  $L_z = 0.3$ . A bi-global stability analysis by Meneghini et al. for a NACA0012 wing section at  $\alpha = 20$  deg revealed a global secondary instability. [25] For a limited spanwise wavenumber range, 3-D instability modes were amplified. Such an instability analysis is beyond the scope of the present paper. However, it must be concluded that relevant 3-D modes may be suppressed when the domain width is too small. The suppression of such 3-D modes affects the momentum exchange and will therefore also have an impact on the mean flow. For example, iso-contours of the streamfunction (Fig. 9) indicate that the “core” of the reverse flow vortex (recirculation) is farther away from the wall for  $L_z = 0.3$  compared to  $L_z = 0.15$ . However, the size and shape of the separated flow region and hence the inviscid outer flow are very similar. As a result, the wall pressure and skin friction coefficient distributions remain almost unchanged (Fig. 6). The conclusion is that the mean flow is predicted accurately as long as the spanwise vortices resulting from the primary instability are captured correctly. This appears to be the case for the narrow computational domain.

A domain width investigation was also carried out for  $\alpha = 30$  deg (Figs. 10 & 11). The spanwise wavelength of the curvature of the separation line is identical to the domain width again indicating that 3-D modes may be altered or suppressed on the narrow domain. However, as for  $\alpha = 20$  deg, neither the size and shape of the separated flow region (Fig. 11) nor the wall pressure and skin friction coefficient distributions (Fig. 6) are affected significantly when the spanwise domain width is changed. Again, the narrow computational domain is sufficient for capturing the primary instability and for providing accurate mean flow predictions.

### 3.1.3. Lift and Drag Data

Finally, a comparison of the lift and drag data with XFOIL and experimental data by Thake et al. [7] is provided in Figs. 12 and 13. As mentioned in the introduction the modified airfoil has a higher maximum lift coefficient than the original NACA airfoil. For the original airfoil, the experimental data

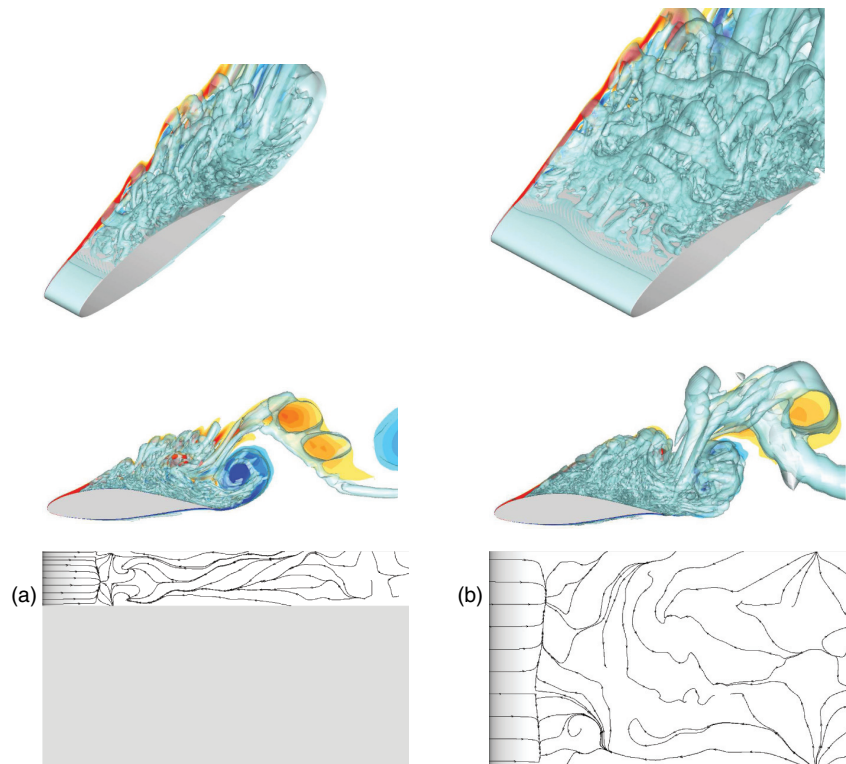


Figure 10. Uncontrolled flow for  $\alpha = 30$  deg. Iso-surfaces of  $Q = 1$ , iso-contours of spanwise vorticity,  $-20 < \omega_z < 20$ , and wall skin friction lines for (a)  $L_z = 0.15$  and (b)  $L_z = 0.6$ .

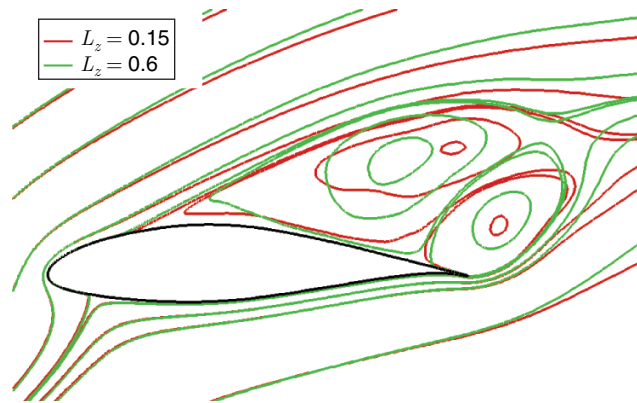


Figure 11. Uncontrolled flow. Streamfunction iso-contours for  $\alpha = 30$  deg.

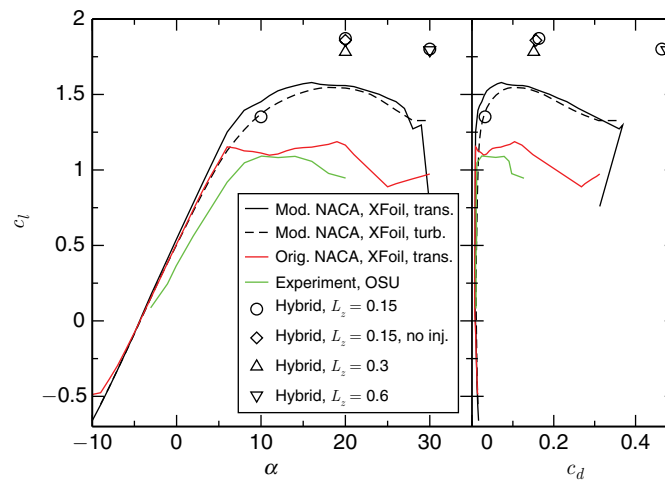


Figure 12. Lift curve and drag polar. Experimental data by Thake et al. [7]

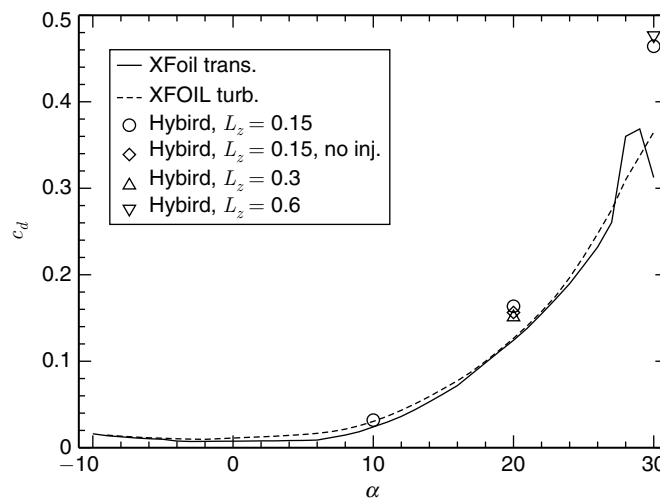


Figure 13. Drag curve.

show a reduced lift slope for  $\alpha < 5$  deg compared to the XFOIL prediction, which may be a result of the low aspect ratio of one in the experiments. The turbulent XFOIL result for  $\alpha = 10$  deg is in good

agreement with the hybrid simulation data. As the angle of attack is increased the XFOil predictions begin to deviate more from the hybrid simulation data. For  $\alpha = 20$  deg lift and drag are under-predicted by 15% and 22% compared to the hybrid data, respectively; For  $\alpha = 30$  deg lift and drag are under-predicted by 36% and 31%, respectively.

### 3.2. Controlled Flow

Earlier research on laminar separation control showed that the shear-layer instability can be exploited for generating spanwise vortices in the separated region. The resulting increased wall-normal mixing leads to a transport of high-momentum freestream fluid towards the wall, thus reducing the extent of the separation or even completely eliminating it. [1, 2, 4] For  $\alpha = 10$  active flow control by harmonic blowing,

$$v = A \frac{1}{2} [1 + \cos(2\pi ft)], \quad (13)$$

through a spanwise slot with amplitude,  $A$ , was investigated. Two pitch angles,  $\varphi = 30$  deg and 90 deg (wall normal blowing), were considered. The spanwise velocity component was zero (zero skew angle).

The slot was modeled by a wall boundary condition for the velocity components. The wall-normal derivatives of the pressure and temperature were set to zero. In the downstream direction, the slot was resolved by 3 cells. This resolution is too low for capturing the detailed fluid dynamics near the slot. This was considered acceptable since the small-scale fluid dynamics are modeled with the chosen hybrid simulation strategy. By setting appropriate dimensionless parameters, such as amplitude, frequency, and momentum coefficient, the integral effect of the forcing is represented in the simulations. The momentum coefficient for harmonic blowing through a slot with width  $\Delta s$  is,

$$c_\mu = \frac{\int \int \left( \frac{1}{T} \int \rho v^2 dt \right) ds dz}{\frac{1}{2} \rho_\infty v_\infty^2 c L_z} = \frac{3}{4} A^2 \Delta s \sin \varphi. \quad (14)$$

The slot location,  $x_s$ , slot width,  $\Delta s$ , blowing frequency,  $f$ , blowing ratio,  $A$ , pitch angle,  $\varphi$ , and momentum coefficient,  $c_\mu$ , are provided in Tab. 4. As a reference, Seifert et al. [26] employed pulsed wall-tangential blowing through a slot for post-stall separation control on a NACA0015 airfoil at  $Re = 0.9$  million. With a momentum coefficient of  $c_\mu = 2.5 \times 10^{-3}$  a 50% lift increase was achieved for  $\alpha = 16$  deg.

Wall-normal ( $\varphi = 90$  deg) harmonic blowing with  $A = 0.1$  was considered first. Flow visualizations (Fig. 14) for  $\alpha = 10$  deg reveal spanwise coherent structures for blowing with  $f = 4$  that are likely a consequence of the actuation. With flow control the separation line becomes straight. It may be conjectured that 3-D mechanisms that are responsible for the spanwise distortion of the separation line for the uncontrolled case are suppressed as a consequence of the 2-D coherence of the flow structures that are introduced by the flow control. Iso-contours of the streamfunction (Fig. 15) indicate a widening of the separated flow region compared to the uncontrolled flow which is reflected in a slightly earlier separation compared to the uncontrolled flow (Fig. 16).

Table 4. Dimensionless flow control parameters.

$x_s$	$\Delta s$	$f$	$A$	$\varphi$	$c_\mu$
0.614	0.0147	1 & 4	0.1	90 deg	$1.10 \times 10^{-4}$
		1 & 4	1	30 deg	$5.51 \times 10^{-3}$

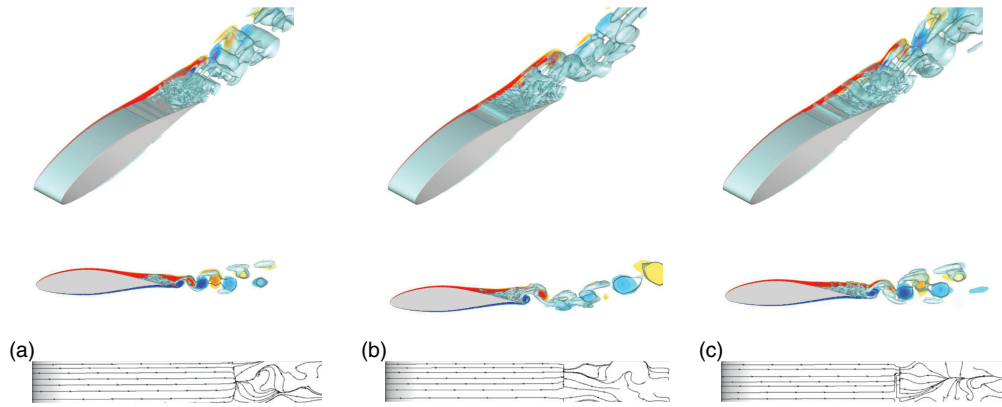


Figure 14. (a) Uncontrolled flow for  $\alpha = 10$  deg. (b), (c) Controlled flow for  $\alpha = 10$  deg with  $A = 0.1$ ,  $\varphi = 90$  deg and (b)  $f = 1$  and (c)  $f = 4$ . Iso-surfaces of  $Q = 1$ , iso-contours of spanwise vorticity,  $-20 < \omega_z < 20$ , and wall skin friction lines.

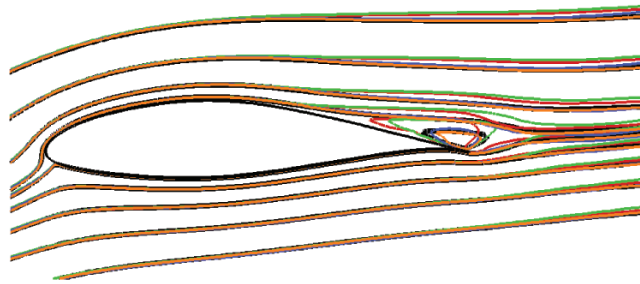


Figure 15. Uncontrolled flow (black) and controlled flow with  $A = 0.1$ ,  $\varphi = 90$  deg and  $f = 1$  (red) and  $f = 4$  (green). Streamfunction iso-contours for  $\alpha = 10$  deg.

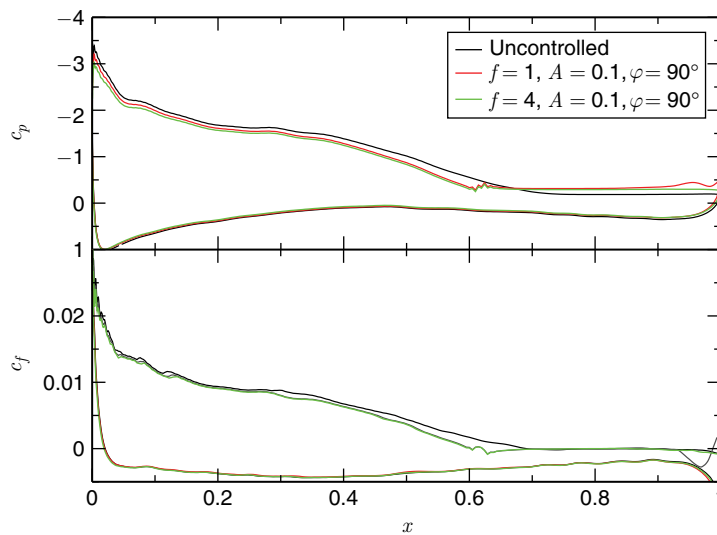


Figure 16. Wall pressure and skin friction coefficient for  $\alpha = 10$  deg.

Figure 17 provides time-histories and Fourier transforms in time of the spanwise average of the skin friction coefficient,  $\bar{c}_f$ . The time-histories reveal that the time-dependent actuation introduces 2-D modes

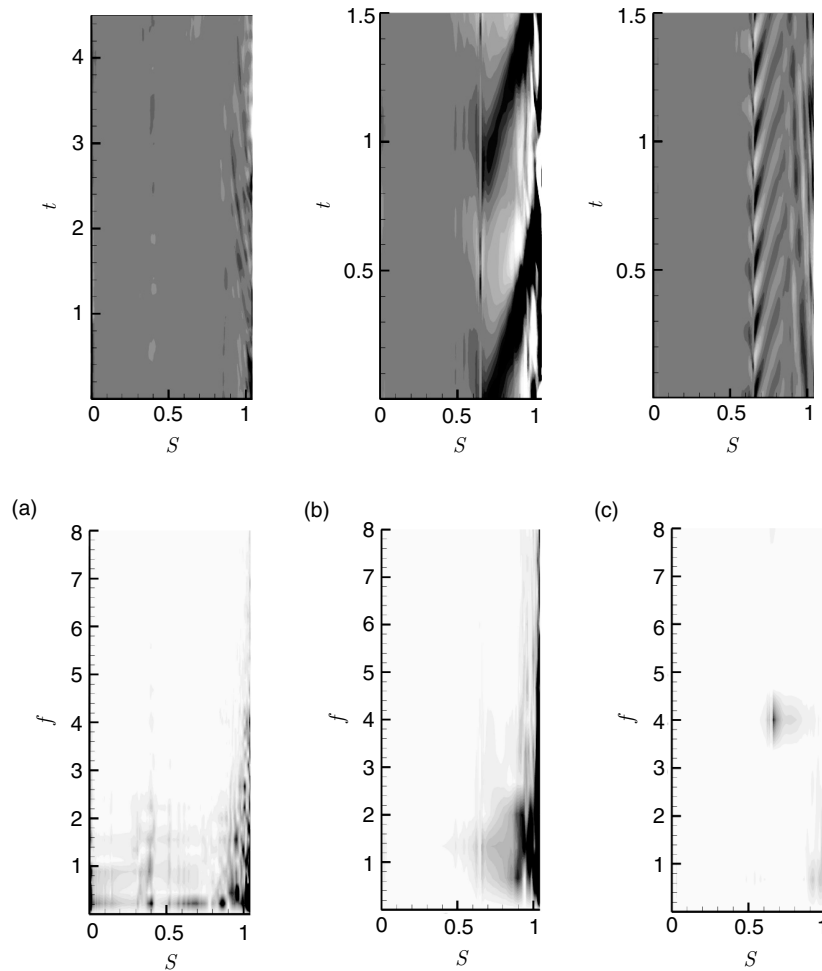


Figure 17. (a) Uncontrolled flow for  $\alpha = 10$  deg. (b), (c) Controlled flow for  $\alpha = 10$  deg with  $A = 0.1$  and (b)  $f = 1$  and (c)  $f = 4$ . Top: Iso-contours of  $-0.001 < \bar{c}_f < 0.001$ . Bottom: Iso-contours of (a)  $0 < A(\bar{c}_f) < 0.0001$ , (b), (c)  $0 < A(\bar{c}_f) < 0.001$ .

that are convected in the downstream direction. The frequency spectra for the uncontrolled flow indicate weak amplification of the disturbance input downstream of separation for  $f = 1$  but not for  $f = 4$ .

By reducing the pitch angle,  $\varphi$  the injected momentum becomes more wall-tangential. By adding downstream momentum near the wall the retarded boundary layer upstream of separation can be re-energized. Preliminary Two-dimensional calculations were carried out for  $A = 1$  and  $\varphi = 30$  deg. Instantaneous visualizations of the unresolved eddy viscosity and spanwise vorticity are shown in Fig. 18. With flow control the separated boundary layer “rolls up” into spanwise coherent structures. This behavior is qualitatively similar to earlier results for  $Re = 64,200$  [4].

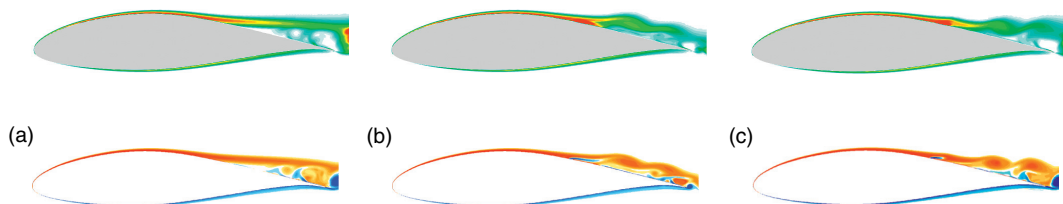


Figure 18. 2-D calculations for  $\alpha = 10$  deg. (a) Uncontrolled flow. (b), (c) Controlled flow with  $A = 1$ ,  $\varphi = 30$  deg and (b)  $f = 1$  and (c)  $f = 4$ . Iso-contours of unresolved eddy viscosity,  $0 < \mu_T < 40$ , (top) and spanwise vorticity,  $-70 < \omega_z < 70$  (bottom).

Figure 19 indicates a dominant frequency of 3.2 for the uncontrolled flow. For flow control with  $f = 1$  a wide range of frequencies is amplified downstream of separation. For  $f = 4$  only the fundamental ( $f = 4$ ) reaches a significant amplitude. Figure 20a provides a more quantitative comparison. The amplitude growth of the primary disturbance in the upstream part of the bubble is very weak (e.g., factor 2.8 for forcing with  $f = 4$ ). This is in contrast to earlier low-Reynolds number results where amplifications of several orders of magnitude were observed. [1, 2, 4] The maximum unresolved eddy viscosity in the separated boundary layer is about 40 (Fig. 18). This lowers the effective Reynolds number and makes the flow less unstable or even stable with respect to 2-D disturbances. Overall, with flow control a slightly larger pressure recovery is obtained (Fig. 20b). If similar results can be reproduced in 3-D simulations will be investigated in the future.

### 3.2.1. Lift and Drag Data

Figure 21 provides a comparison of the time-averaged lift and drag data with XFOIL results. For the wall-normal injection ( $\varphi = 90$  deg) with  $A = 0.1$  lift is reduced and drag is increased.

The pitched injection ( $\varphi = 30$  deg) with  $A = 1$  leads to a slight lift increase and a drag reduction. Time histories of the lift and drag coefficient are shown in Fig. 22. With control the lift coefficient is modulated by the frequency of the actuation indicating that the circulation around the entire wing section “locks in” to the actuation. Overall with flow control aerodynamic performance (lift over drag) is only mildly increased or (if the parameters are not chosen right) considerably diminished (Tab. 5). Future research will have to show (1) why harmonic blowing through a slot, which was found to work

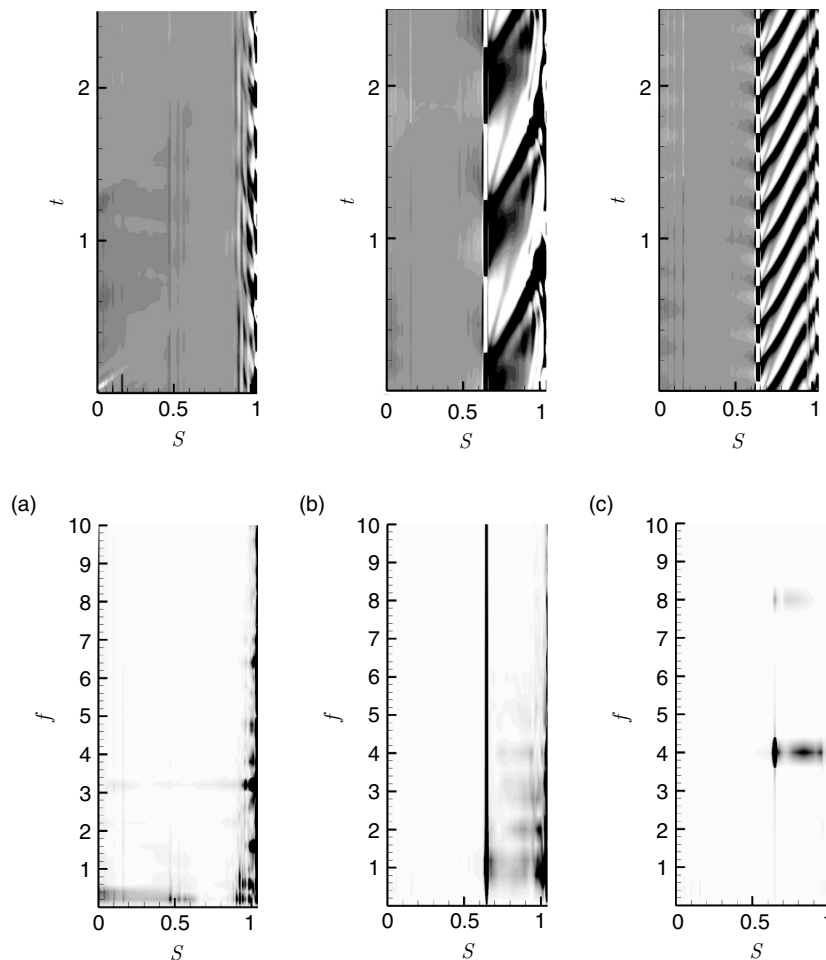


Figure 19. 2-D calculations for  $\alpha = 10$  deg. (a) Uncontrolled flow. (b), (c) Controlled flow with  $A = 0.1$  and (b)  $f = 1$  and (c)  $f = 4$ . Top: Iso-contours of  $-0.001 < \bar{c}_f < 0.001$ . Bottom: Iso-contours of (a)  $0 < A(\bar{c}_f) < 0.0002$ , (b), (c)  $0 < A(\bar{c}_f) < 0.002$ .

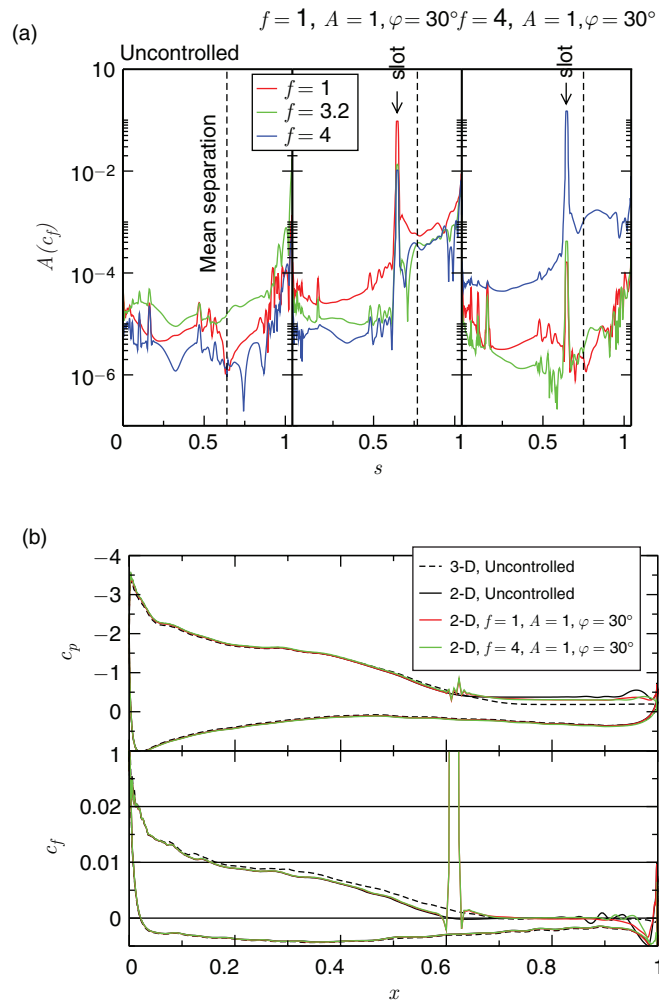


Figure 20. 2-D calculations for  $\alpha = 10$  deg. (a) Skin friction disturbance amplitudes and (b) Wall pressure and skin friction coefficient.

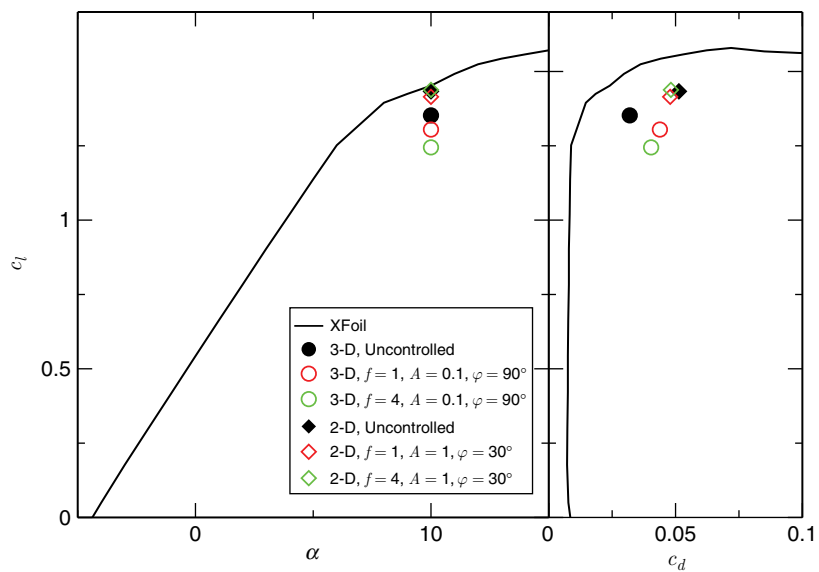


Figure 21. Lift curve and drag polar.

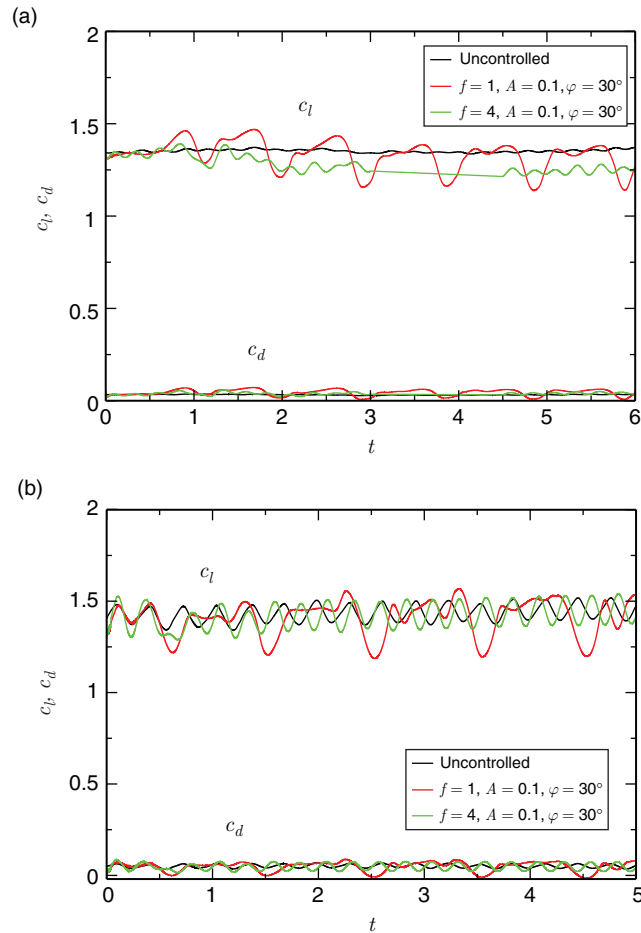


Figure 22. Time histories of lift and drag coefficient obtained from (a) 3-D simulations and (b) 2-D calculations.

Table 5. Lift and drag coefficient and aerodynamic performance.

case	$C_l$	$C_d$	$C_l/C_d$	$C_l/C_d$ change
3-D, uncontrolled	1.35	0.0319	42.3	
3-D, $f = 1$ , $A = 0.1$ , $\varphi = 90$ deg	1.30	0.0438	29.8	-30%
3-D, $f = 4$ , $A = 0.1$ , $\varphi = 90$ deg	1.24	0.0404	30.8	-27%
2-D, uncontrolled	1.43	0.0513	27.9	
2-D, $f = 1$ , $A = 1$ , $\varphi = 30$ deg	1.41	0.0479	29.5	+6%
2-D, $f = 4$ , $A = 1$ , $\varphi = 30$ deg	1.44	0.0482	29.9	+7%

well for low-Reynolds number applications, [1, 2, 4] is less effective for  $Re = 1$  million and (2) what other flow control strategies may fare better.

#### 4. CONCLUSION

A one-equation hybrid turbulence model in combination with a procedure that introduces turbulent velocity fluctuations were employed for wing section simulations at  $Re = 1$  million. Simulations of the uncontrolled flow for  $\alpha = 10$  deg are in good agreement with XFOil data. As the angle of attack is increased to 20 and 30 deg the XFOil lift and drag predictions begin to deviate more and more from the hybrid turbulence model results. These discrepancies may be attributed to problems with the XFOil

predictions in the post-stall regime or to possible turbulence modeling issues. To address the latter, other hybrid models (e.g., based on two equation turbulence models and/or explicit algebraic stress models) will be considered in the future. Should wind tunnel data become available they will provide an opportunity for the validation of the hybrid simulations.

Active flow control by harmonic blowing through a spanwise slot was found to be only mildly effective or even counterproductive. In particular, the disturbances that were introduced by the control were only weakly amplified or dampened. This came as a surprise as similar flow control strategies worked well for low-Reynolds number applications. [1,2,4] The maximum unresolved eddy viscosity in the separated boundary layer for the present simulations was about 40. This lowers the effective Reynolds number and makes the flow less unstable or even stable with respect to 2-D disturbances. As a result, higher blowing ratios are required compared to flow control at low-Reynolds number conditions where the shear-layer instability is stronger.

In the future, flow control strategies that exploit different physical mechanisms or combinations thereof will be considered (e.g., steady and pulsed vortex generator jets). The hybrid turbulence model employed for the present investigations may provide too much model contribution and thus inhibit instability mechanisms. For validation purposes, future flow control simulations will also be based on other hybrid models and results will be compared with experimental data when available.

## ACKNOWLEDGMENTS

This work was funded by the Air Force Office of Scientific Research (AFOSR) under grant number FA9550-09-1-0214 with Dr. Douglas Smith serving as program manager. High Performance Computing (HPC) resources were provided by the Department of Defense HPC Modernization Program. This work was supported in part by a grant of HPC resources from the Arctic Region Supercomputing Center.

## NOMENCLATURE

$A$	forcing amplitude, mode amplitude
$c$	chord length
$c_d$	drag coefficient
$c_f$	skin friction coefficient
$c_l$	lift coefficient
$c_\mu$	momentum coefficient
$E(k)$	energy spectrum
$f$	forcing frequency
$k$	turbulence kinetic energy
$l$	streamwise spacing of spanwise vortices
$l_T$	integral turbulence length scale
$L_k$	Kolmogorov length scale
$L_z$	spanwise grid extent
$L_\Delta$	grid length scale
$p$	pressure
$P_k$	$k$ production term
$Q$	vortex identification criterion
$S_{ij}$	strain tensor
$s$	arc-length along suction surface measured from leading edge
$t$	time
$Tu$	turbulence intensity
$u, v, w$	velocity components
$u^+$	velocity in wall units
$u_\tau$	friction velocity
$W_{ij}$	rotation tensor
$x, y, z$	coordinates
$x_s$	forcing slot location
$y$	wall distance
$y^+$	wall distance in wall units
$\alpha$	angle of attack

$\delta_{i,j}$	Kronecker symbol
$\Delta s$	slot width
$\Delta t$	computational timestep
$\varepsilon$	turbulence dissipation rate
$k$	wave number
$\mu$	dynamic viscosity
$\mu_T$	eddy viscosity
$\nu$	kinematic viscosity
$\rho$	density
$\tau_{ij}^T$	Reynolds stress
$\varphi$	jet pitch angle
$\Psi$	streamfunction
$\omega_z$	spanwise vorticity

## REFERENCES

- [1] Postl, D., Balzer, W., and Fasel, H.F., "Control of laminar separation using pulsed vortex generator jets: direct numerical simulations," *Journal of Fluid Mechanics*, 2011, 676, 81–109
- [2] Gross, A., and Fasel, H.F., "Numerical simulation of low-pressure turbine blade separation control," *AIAA Journal*, 2010, 48(8), 1582–1601
- [3] Bons, J.P., Sondergaard, R., and Rivir, R.B., "Turbine Separation Control Using Pulsed Vortex Generator Jets," *Journal of Turbomachinery*, 2001, 123(2), 198–206
- [4] Gross, A., and Fasel, H.F., "Active flow control for NACA 6-series airfoil at  $Re = 64,200$ ," *AIAA Journal*, 2010, 48(9), 1889–1902
- [5] Mack, S., Brehm, C., Heine, B., and Fasel, H., "Experimental investigation of separation and separation control of a laminar airfoil," *AIAA-paper AIAA-2008-3766*, June 2008
- [6] Plogmann, B., Mack, S., and Fasel, H., "Experimental Investigation of Open- and Closed-Loop Control for Airfoil Under Low Reynolds Number Conditions," *AIAA-paper AIAA-2009-4282*, June 2009
- [7] Thake, M., Packard, N., Bonilla, C., Gompertz, K., and Bons, J., "Reynolds Number Scalability for Separation Control on a Laminar Airfoil," *AIAA-paper AIAA-2011-1182*, Jan. 2011
- [8] Gross, A., Pearman, C., Kremer, R., Napier, B., Gosla, C., Kurz, A., Mack, S., Brehm, C., Heine, B., Radi, A., Marovic, B., Retzko, S., Feindler, N., Zickler, B., Fasel, H.F., and Osbrink, A., "1/5 Scale Model of Aeromot 200S SuperXimango for Scaled Flight Research," *AIAA-paper AIAA-2008-6416*, Aug. 2008
- [9] Heine, B., Mack, S., Kurz, A., Gross, A., and Fasel, H.F., "Aerodynamic Scaling of General Aviation Airfoil for Low Reynolds Number Application," *AIAA-paper AIAA-2008-4410*, June 2008
- [10] Brehm, C., Mack, S., Gross, A., and Fasel, H., "Investigation of an Airfoil at Low Reynolds Number Conditions," *AIAA-paper AIAA-2006-3765*, June 2008
- [11] Gross, A., and Fasel, H., "Numerical Investigation of Separation for Airfoils at Low Reynolds Numbers," *AIAA-paper AIAA-2010-4736*, June 2010
- [12] Gross, A., and Fasel, H.F., "Numerical Investigation of Separation for Airfoils," *AIAA-paper AIAA-2011-3438*, June 2011
- [13] De Langhe, C., Bigda, J., Lodefier, K., and Dick, E., "One-Equation RG Hybrid RANS/LES Modelling," *Adv. in Hybrid RANS-LES Modelling*, eds. S.-H. Peng and W. Haase, NNFM 97, Springer, 2008, 97–106
- [14] De Langhe, C., Bigda, J., Lodefier, K., and Dick, E., "One-equation RG hybrid RANS/LES computation of a turbulent impinging jet," *Journal of Turbulence*, 2008, 9(16), 1–19
- [15] Giles, M.J., "Turbulence renormalization group calculations using statistical mechanics methods," *Physics of Fluids*, 1994, 6(2), 595–604
- [16] Batten, P., Goldberg, U., and Chakravarthy, S., "Interfacing Statistical Turbulence Closures with Large-Eddy Simulation," *AIAA Journal*, 2004, 42(3), 485–492
- [17] Rogallo, R., "Numerical experiments in homogeneous turbulence," NASA Technical Report TM-81315, 1981

- [18] Gross, A., and Fasel, H.F., “High-Order-Accurate Numerical Method for Complex Flows,” *AIAA Journal*, 2008, 46(1), 204–214
- [19] Gross, A., and Fasel, H.F., “Characteristic Ghost-Cell Boundary Condition,” *AIAA Journal*, 2007, 45(1), 302–306
- [20] Gross, A., and Fasel, H.F., “Multi-block Poisson grid generator for cascade simulations,” *Mathematics and Computers in Simulation*, 2008, 79(3), 416–428
- [21] Reichardt, H., “Vollständige Darstellung der turbulenten Geschwindigkeitsverteilung in glatten Leitungen,” *ZAMM - Journal of Applied Mathematics and Mechanics / Zeitschrift für Angewandte Mathematik und Mechanik*, 1951, 31(7), 208–219
- [22] Drela, M., and Giles, M.B., “Viscous-inviscid analysis of transonic and low Reynolds number airfoils,” *AIAA Journal*, 1987, 25(10), 1347–1355
- [23] Pierrehumbert, R., and Widnall, S., “The two- and three-dimensional instabilities of a spatially periodic shear layer,” *Journal of Fluid Mechanics*, 1982, 114, 59–82
- [24] Hunt, J.C.R., Wray, A.A., and Moin, P., “Eddies, stream, and convergence zones in turbulent flows,” Report CTR-S88, Center For Turbulence Research, Stanford, California, 1988
- [25] Meneghini, J.R., Carmo, B.S., Tsiloufas, S.P., Gioria, R.S., and Aranha, J.A.P., “Wake instability issues: From circular cylinders to stalled airfoils,” *Journal of Fluids and Structures*, 2011, 27(5), 694–701
- [26] Seifert, A., Greenblatt, D., and Wygnanski, D.J., “Active separation control: an overview of Reynolds and Mach numbers effects,” *Aerospace Science and Technology*, 2004, 8(7), 569–582

